THE JOURNAL OF PHYSICAL CHEMISTRY C
A JOURNAL OF THE AMERICAN CHEMICAL SOCIETY

pubs.acs.org/JPCC

Article

From Insulator to Metal: Theoretical Assessment on the Optical Properties of Vanadium Dioxide Using Many-Body First-Principles Approaches

Zafer Kandemir, Claudia Cardoso, Pino D'Amico, Cem Sevik,* and Kürşat Şendur*

Cite This: https://doi.org/10.1021/acs.jpcc.5c03003

Read Online

ACCESS | Metrics & More | Article Recommendations | Supporting Information

ABSTRACT: Vanadium dioxide (VO_2) exhibits a temperature-driven insulator-to-metal transition, making it a promising material for optical and electronic applications. In this study, we perform a systematic first-principles investigation of the electronic and optical properties of VO_2 in its monoclinic (M_1) and rutile (R) phases using density functional theory (DFT), many-body perturbation theory (G_0W_0), and the Bethe-Salpeter equation (BSE). Our results reveal that excitonic effects play a crucial role in accurately describing the dielectric response of the semiconducting M_1 phase, with G_0W_0/BSE and PBE/BSE approaches yielding optical spectra in excellent agreement with experimental data. For the metallic R phase, we find that the random phase approximation (RPA) at the PBE level provides a reliable description of its optical properties, particularly in the visible range, as long as intraband contributions are included. The frequency-dependent dielectric functions presented in this work achieve the required accuracy for large-scale optical simulations relevant to smart coatings and tunable infrared devices. To support further research and applications, we provide our computed optical data in an open-access repository on ZENODO.

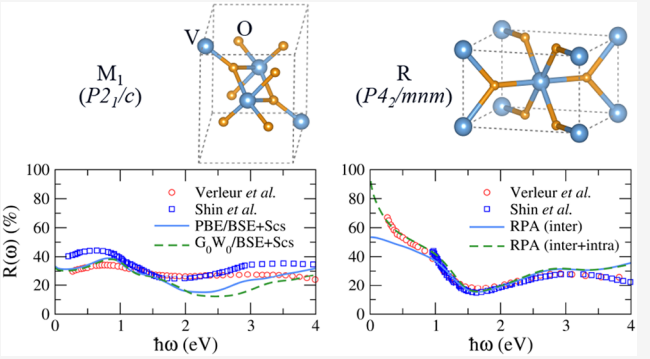

INTRODUCTION

Vanadium dioxide (VO_2) is a metal oxide of growing technological significance due to its structurally driven insulator-to-metal transition (IMT).[1] At low temperatures, VO_2 behaves as an insulator with an experimentally measured band gap of 0.4−0.7 eV,[2,3] forming a monoclinic (M_1) structure with the $P2_1/c$ space group.[4] At around 341 K (68 °C), VO_2 undergoes a transition to a metallic state, adopting a rutile tetragonal structure (R) with the $P4_2/mnm$ space group.[5] Discussed for the first time in 1959,[5] the origin of the abrupt change in resistance with temperature attracted immediate attention,[6] and was the subject of debate for several decades.[7−10] The optical properties were first reported in ref 2 showing, below the transition temperature, four absorption peaks at 0.85, 1.3, 2.8, and 3.6 eV. In the metallic phase, the peaks near 3 and 4 eV are still present, and a free-carrier absorption peak is seen below 2.0 eV. Subsequently, optical measurements were supplemented with other methods such as X-ray photoelectron and Auger spectroscopy[3] and ultraviolet reflectance and photoemission.[11]

The electronic rearrangement during the photoinduced insulator−metal phase transition in VO_2 was studied by femtosecond X-ray absorption spectroscopy by measuring the filling dynamics of differently hybridized V3d-O2p bands.[12] The structural influence on the resistance is also seen in VO_2 films epitaxially grown along different directions[13] Due to the unique physical properties of both phases and the high transition temperature, this material has received significant attention for various applications, including electronic switches and thermal management systems.[14−16] Since the metallic state of VO_2 effectively reflects infrared radiation, considerable research has focused on high-potential applications such as smart optoelectronic devices,[17−21] energy-saving thermochromic coatings for building windows,[22−26] electrochromic screens,[27−29] radiative cooling systems,[30] and adjustable optical functionality through morphology control.[31,32]

Despite the considerable potential of this material for optical applications,[2,33−39] the investigation of its dielectric properties remains limited. For the M_1 phase, the reported experimental results exhibit inconsistencies due to structural variations and the presence of impurities.[2,33−39] Among these, two experimental studies[2,11] provide reflectance data for the M_1 phase that can be used as a reference for first-principles approaches.

Received: May 1, 2025
Revised: September 9, 2025
Accepted: September 9, 2025

In one of these studies, the real (ε_1) and imaginary (ε_2) parts of the dielectric function are estimated by fitting the reflectance data using the Drude and Lorentz models.[2] The same study reports also the only available dielectric data for the R phase. The measured spectrum for light polarization along the V−V dimers is essentially featureless, whereas, perpendicular to the V−V dimers, it shows a large dip between 1 and 3 eV.

From the theory point of view, while there are no results reported on the R phase considering both inter and intraband transitions, the results reported for the M_1 phase fail to fully reproduce the experimental data, and exhibit differences due to the various approximations employed.[40−45] Therefore, a systematic and accurate investigation of the metallic R phase would address critical gaps in understanding the optical properties of the intriguing phases of VO_2.

With this aim, we first performed calculations, including many-body effects, through the GW method for the semiconducting phase of VO_2, in order to provide an understanding of the theoretical framework that best reproduces the experimental results. Subsequently, we investigated the optical properties of the metallic phase, using the random phase approximation (RPA) while including the intraband optical response. Overall, we achieved a good agreement between the theoretical and experimental results, thereby advancing the understanding of the optical properties of VO_2.

COMPUTATIONAL METHODS

In the M_1 phase, VO_2 has a monoclinic structure with a unit cell of 12 atoms, consisting of four vanadium and eight oxygen atoms. In this structure, the vanadium atoms form paired chains along the *c*-axis due to a Peierls-like distortion, resulting in alternating short and long V−V bonds. The quasi-one-dimensional nature of these VO_2 chains plays a crucial role in the electronic properties of the material, leading to strong anisotropy in both transport and optical responses. In contrast, the high-temperature R phase exhibits a tetragonal rutile structure with a unit cell containing six atoms, where vanadium atoms are evenly spaced and the material behaves as a metal. The schematic representation of these crystals is shown in Figure 1,

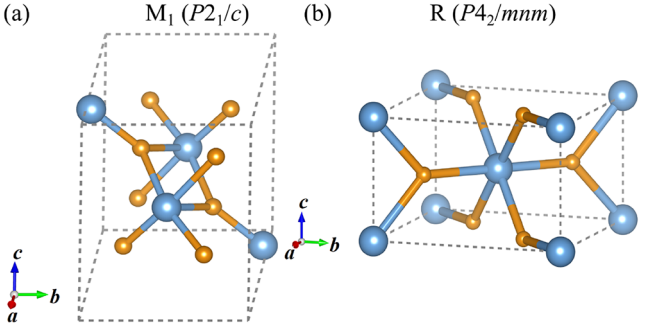

Figure 1. Side view of crystal structures for the M_1 and the R phases of VO_2. Vanadium and oxygen atoms are represented by blue and orange spheres, respectively.

We performed geometric optimization and electronic properties' calculations for both phases of VO_2 by using density functional theory (DFT) as implemented in the Quantum ESPRESSO package.[46,47] The exchange and correlation part of the potential was treated using the generalized-gradient approximation (GGA) with Perdew−Burke−Ernzerhof (PBE).[48,49] We accounted for the van der Waals (vdW) interactions between layers, using the semi-empirical DFT-D2 Grimme method.[50] The electron wave function was expanded in a plane-wave basis set with an energy cutoff of 125 Ry. The convergence tolerance was set as 10^{-10} eV/atom for energy and 0.01 eV/Å for maximum force. For the geometric optimizations of the M_1 and R phases, we used $6 \times 6 \times 6$ and $6 \times 6 \times 12$ *k*-grids, respectively, using the variable-cell relax method. Our results for both phases confirm previous calculations[51] and are in reasonable agreement (within 1%−2%) with experimental predictions.[6,52−55]

In order to include many-body effects in the calculations of the electronic properties, we performed G_0W_0 simulations on top of the PBE result with the YAMBO code.[56,57] Since the M_1 phase is insulating, we chose the plasmon-pole approximation (PPA) for the frequency description of the response function within G_0W_0, whereas for the metallic R phase, we used a full frequency real-axis approach. The band structure and the density of states (DOS) computed using both G_0W_0/PPA and PBE, are presented in Figure S1 for the M_1 phase and in Figure S2 for the R phase.

When calculating the quasi-particle energies for the M_1 phase, a Γ-centered $8 \times 8 \times 8$ *k*-grid was used, corresponding to 260 *k*-points in the irreducible Brillouin zone (IBZ), and more than 450 states were included for both the screening function and Green's function descriptions. For the R phase we used a $6 \times 6 \times 12$ *k*-grid with 91 *k*-points in the IBZ. On both DFT/PBE and GW band structures, we applied a scissors correction in order to better reproduce the experimental band gap. The scissors value was determined by adjusting the position of the first peak in the experimentally reported ε_2 data[2] (more details in Table S1).

The optical properties were obtained both with the independent particle approximation (IPA) and including electron−hole interactions by solving the Bethe-Salpeter equation (BSE)[58] as implemented in the Yambo code. For the M_1 phase, the BSE method was applied on top of both G_0W_0/(PPA) and PBE band structures.

For the R phase, the random-phase approximation (RPA) method was computed on top of the PBE band structure since it already provides a reasonable agreement with the experimentally measured data. Due to the computational efficiency of the RPA method, an $18 \times 18 \times 18$ *k*-grid with 910 *k*-points in the IBZ was used. Given the metallic nature of the R phase, the intraband contribution was calculated and incorporated into the RPA results, as detailed in our previous study.[59]

RESULTS AND DISCUSSION

In order to validate our approach, we start by calculating the dielectric properties of the semiconducting M_1 phase of VO_2, and comparing our results with available reflectance data.[2,11] For this purpose, we computed the reflectance by applying eq 1

$$R(\omega) = \left| \frac{\sqrt{\varepsilon_1(\omega) + i\varepsilon_2(\omega)} - 1}{\sqrt{\varepsilon_1(\omega) + i\varepsilon_2(\omega)} + 1} \right|^2 \quad (1)$$

to the real and imaginary parts of the dielectric function obtained from YAMBO calculations. For the semiconducting phase, we corrected the DFT band structure in two different ways. First, by applying to the DFT band structure a scissors

https://doi.org/10.1021/acs.jpcc.5c03003
J. Phys. Chem. C XXXX, XXX, XXX−XXX

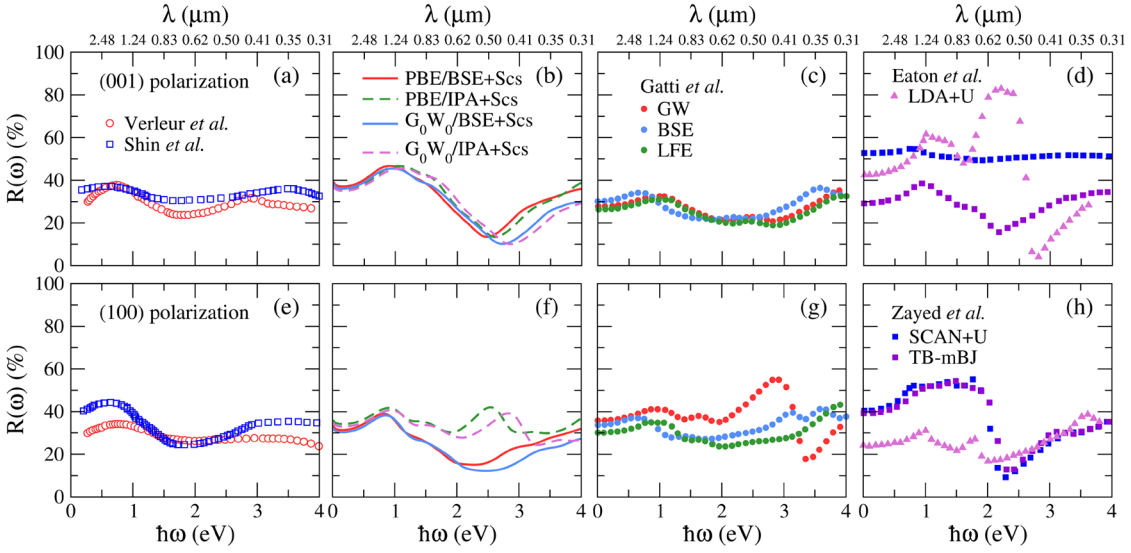

Figure 2. For the M_1 phase, the reflectivity $R(\omega)$ is calculated using eq 1 and compared with the experimental data reported by Verleur et al.[2] and Shin et al.[11] In panels (a–d) the results for the (001) polarization are shown, while in panels (e–h), the results correspond to the (100) polarization. The red solid, green dashed, blue solid and pink dashed lines represent the results of PBE/BSE + Scs, PBE/IPA + Scs, G_0W_0/BSE + Scs and G_0W_0/IPA + Scs, respectively. In panels (c) and (g), the red, blue and green circles correspond to GW, BSE and LFE results, respectively.[42] In Zayed's study, violet and dark-blue squares indicate TB-mBJ and SCAN + U results, respectively.[45] In Eaton's study, pink triangles show LDA + U result.[43].

correction. Second, by including many body effects through a one-shot G_0W_0 calculation. However, the GW band structure is not enough to reproduce the experimentally reported band gap of M_1 VO_2 and therefore we further corrected the band structure with a scissors operator. In both DFT and GW calculations, the value of the scissors (Scs) correction was determined by adjusting the position of the first peak in the experimentally reported ε_2 data.[2] This approach yielded a band gap of 0.51 eV for PBE and 0.54 eV for G_0W_0. The estimated band gaps, along with experimental values (0.4–0.7 eV),[2,3,6−13] are summarized in Table S1.

In the panels (b) and (f) of Figure 2 we show the calculations done within different levels of theory. The optical spectra were then computed both at the IPA and the BSE level. Both for the spectra obtained with IPA and BSE, the plots show that the computationally more efficient PBE + Scs approach yields results similar to those obtained from many-body G_0W_0 calculations. This could be explained by the fact that both calculations use the same DFT wave function, since the G_0W_0 procedure corrects only the energy levels. Moreover, since both DFT and GW energies were further corrected with a scissors operator, we do not expect significant differences. The results computed with IPA shown in Figure 2b,f, show a strong anisotropy of the calculated reflectivity spectrum, with a well-defined peak around 2.5 eV for the (100) polarization, that is absent for (001). This peak is also absent in the experimental measurements. In contrast, for the (001) direction, the IPA calculations show overall good agreement with experiment, although the calculated optical response exhibits a more pronounced dip that is shifted to higher energies.

If we now compare the IPA and BSE spectra, we see a significant difference only for the (001) polarization. In fact, the BSE spectra are now in much better agreement with the experiment, exhibiting a dip around 2.5 eV, where previously a peak was observed.

In Figure 2c,d,g,h we present the reflectance derived using eq 1 from previously reported calculations of the dielectric function.[42,43,45] Zayed et al. reported reflectance data obtained using the TB-mBJ and SCAN + U methods.[45] Their findings indicate that SCAN + U closely reproduces the experimental data for the (001) polarization, whereas the TB-mBJ method yields higher reflectance values, deviating significantly from the experiment. Similarly, Eaton's LDA + U calculations show an overestimation of reflectance for the (001) polarization and an underestimation for the other polarization.[43]

Gatti et al.[41] reports calculations using the GW, BSE, and local-field effect (LFE) methods for both polarization directions. The BSE results are in good agreement with experiment and are very similar to our present findings. The differences are mainly the slightly lower magnitudes, that can be explained by the fact that, the BSE calculation in ref 41 (Gatti et al.) was done on top of a combination of self-consistent COHSEX and one-step G_0W_0, which updates, with respect to DFT, not only the energies but also the wavefunctions.

The peaks observed in the G_0W_0-BSE spectra correspond to transitions between the valence V-3d states just below the Fermi level and the conduction V-3d states near 1 eV, as illustrated in the G_0W_0 band structures of the M_1 phase in Figure S1. Additionally, the final peak around 3.5–4.0 eV arises from transitions between the valence O-2p bands (located between −1.25 and −2.50 eV) and the conduction V-3d states near 1.50 eV. These spectral features are also observed in the PBE-BSE case, albeit with slight energy shifts.

As already discussed in ref 41 (Gatti et al.), the anisotropy observed in the VO_2 spectra of the M_1 phase due to excitonic effects can be explained by the nature of the transitions involved. The peak shown at the IPA level is due to transitions between t_{2g} states oriented along the direction of the V–V dimers, which form a one-dimensional band in the solid. An applied field along the dimer direction will create induced fields in the opposite direction, resulting in a depolarization

https://doi.org/10.1021/acs.jpcc.5c03003
J. Phys. Chem. C XXXX, XXX, XXX−XXX

effect. These crystal local-field effects are only included in the BSE, while neglected in the IPA calculations. Besides the crystal field effects, BSE also includes excitonic effects that further improve the agreement with experiments.

We now focus on the metallic R phase. The calculated reflectance spectra for electric field (100) and (001) polarizations are shown in Figure 3, in comparison with the

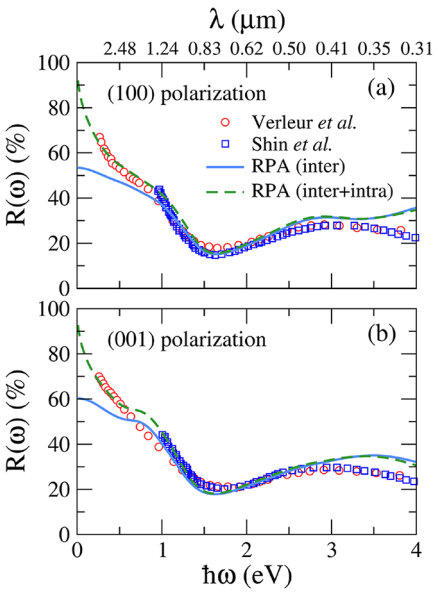

Figure 3. For R phase, the reflectivity, $R(\omega)$ is calculated using eq 1 and compared with the experimental data reported by Verleur et al.[2] and Shin et al.[11] The polarization of the electric field is along (a) the (100) direction and (b) the (001) direction, respectively. The blue solid and green dashed lines represent the results of RPA (inter) and RPA (inter + intra), respectively.

respective experimental results. The spectra are characterized by a minimum around 1.5 eV and a broad maximum above 3 eV, with almost no difference between the two polarizations.

The excitonic effects, as expected for a metallic phase, are less important in this case. The crystal structure also exhibits a three-dimensional character, which results in reduced anisotropy. The RPA method effectively describes interband contributions in both polarization directions, except in the 0−1 eV range, where intraband transitions dominate. To account for this, we estimate the intraband contribution using a Drude-model-based approach. The inclusion of this contribution leads to good agreement with experimental data, representing the best agreement reported in the literature to date.[44,60]

To quantify this agreement in detail, we evaluated the relative error between the theoretical and experimental reflectivity spectra for the metallic R phase along the (100) and (001) crystallographic directions, defined as

$$\text{relative error} = \frac{\left\| R_{\text{exp}} - R_{\text{theory}} \right\|_2}{\left\| R_{\text{exp}} \right\|_2} \tag{2}$$

where $\|\cdot\|_2$ denotes the 2-norm of the reflectivity vector. As summarized in Table 1, for the (100) direction the relative error decreases from 16% (interband only) to 9% (inter + intraband), while for the (001) direction it is reduced from 14% to 9%. In the infrared region (0−1.55 eV), dominated by

Table 1. Relative Error between the Calculated and Experimental Reflectivity Spectra for the Metallic R Phase of VO_2 along the (100) and (001) Directions

	(100) direction		(001) direction	
	RPA (inter)	RPA (inter + intra)	RPA (inter)	RPA (inter + intra)
total relative error (all energies)	16%	9%	14%	9%
infrared (0−1.55 eV)	15%	5%	13%	7%
UV−visible (1.55−3.1 eV)	9%	10%	10%	11%
deep UV (3.1−4.0 eV)	22%	22%	27%	25%

intraband contributions, the error reduction is particularly pronounced from 15% to 5% for the (100) direction and from 13% to 7% for the (001) direction. In the UV−visible range (1.55−3.1 eV), the errors remain below 11% for both orientations, whereas in the deep-UV region (3.1−4.0 eV), they lie between 22% and 27%.

Overall, the inclusion of intraband effects consistently improves the quantitative agreement with experiment, with especially low relative errors in the infrared regime. These results demonstrate that for the metallic R phase, frequency-dependent optical response functions obtained at the RPA level already provide sufficient accuracy for use in large-scale optical simulations, consistent with expectations for metallic systems.

Dielectric Function of M_1 and R Phases. As discussed in the previous section, we have implemented a computational framework that reproduces the experimental reflectance of both semiconducting and metallic VO_2. Here, we look in more detail at each of the real (ε_1) and imaginary (ε_2) components of the dielectric function for each crystalline phase.

Usually, ε_1 and ε_2 are determined empirically from measured reflection spectra, relying on various models, including the Lorentz, Drude, and Gaussian models,[2,33,34,38] along with assumptions about the high-frequency dielectric constant. For the M_1-phase VO_2, Verleur et al. extracted ε_1 and ε_2 using the Lorentz and Drude models. Taking a closer look, we realized that the reported values do not satisfy the Kramers−Kronig (KK) relations, which could make the comparison with the calculations difficult. To quantify this discrepancy, we extended Verleur's ε_2 data up to 10 eV employing a combined Drude−Lorentz model in which the first term accounts for the Drude contribution, while the second term represents interband transitions modeled via multiple Lorentz oscillators. corresponding to the following parametrization

$$\varepsilon_2(\omega) = \frac{\gamma\omega_p^2}{\omega^3 + \omega\gamma^2} + \sum_{i=1}^{n} \frac{s_i \Gamma_i \frac{\omega}{\omega_i}}{\left(1 - \frac{\omega^2}{\omega_i^2}\right)^2 + \Gamma_i^2 \frac{\omega^2}{\omega_i^2}} \tag{3}$$

where ω_p is the plasma frequency, γ the collision frequency, s_i the i-th oscillator strength, ω_i its frequency, and Γ_i its linewidth. Since the M_1 phase is semiconducting, the first term is necessarily zero and the optical response is thus described solely by multiple Lorentz oscillators accounting for interband transitions. The full set of fitting parameters used in this expression is summarized in Table 2.

Subsequently, we determined the ε_1 values using the extended data presented in Figure 4 and the KK equation

https://doi.org/10.1021/acs.jpcc.5c03003
J. Phys. Chem. C XXXX, XXX, XXX−XXX

Table 2. Fitting Parameters Used in Eq 3 to Reproduce Verleur's $\varepsilon_2(\omega)$ Spectrum[2]

s_i	ω_i (eV)	Γ_i
0.884	5.820	0.560
0.866	4.360	0.390
0.747	3.800	0.365
0.482	3.420	0.260
0.490	2.970	0.150
1.156	1.510	0.550
1.274	1.190	0.530
1.722	0.960	0.480
1.990	0.770	0.520

$$\varepsilon_1(\omega) = 1 + \frac{2}{\pi}\mathcal{P}\int_0^\infty \frac{\omega'\varepsilon_2(\omega')}{\omega'^2 - \omega^2}\mathrm{d}\omega' \quad (4)$$

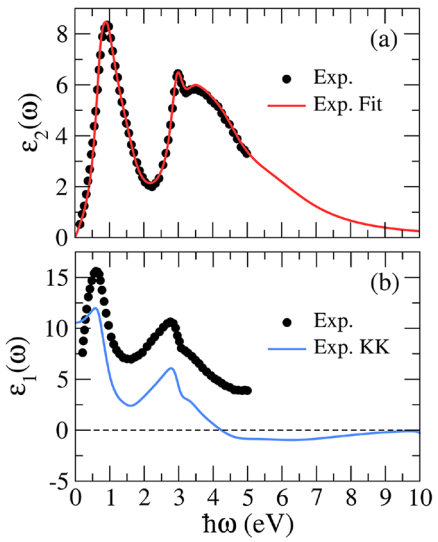

Figure 4. Imaginary and the real parts of the dielectric function of VO_2 in the M_1 phase for the bulk structure, obtained experimentally (black circles).[2] (a) Fitting result obtained using eq 3 (red line). (b) Result of Kramers–Kronig (KK) analysis using the fitted data (blue line).

Here, $\mathcal{P}$ denotes the principal value, which ensures a well-defined result by properly handling singularities in the integral. As shown in Figure 4b, the ε_1 values reported by Verleur et al. do not match those obtained via the Kramers–Kronig relation. In particular, around 0.5 eV, the difference between the experimental and the theoretical values is approximately 3, while between 1 and 5 eV, it increases to a value of 5. We attribute this deviation to the fitting methods employed. Similar inconsistencies are common in experimental studies.

Figure 5 presents the calculated dielectric properties obtained using the PBE/BSE + Scs, PBE/IPA + Scs, G_0W_0/BSE + Scs, and G_0W_0/IPA + Scs approximations, alongside available experimental data. Given the orthorhombic crystal symmetry, we present results separately for each crystallographic direction. The calculations show reasonable agreement with ε_2, while ε_1 exhibits a notable underestimation above 1.5 eV when compared directly with the reported experimental data. If we instead compare with the ε_1 determined from the KK transformation of ε_2, the agreement significantly improves. Notably, our calculated values of ε_1 along the (100) direction show excellent agreement with the KK-corrected experimental measurements, as illustrated in Figure 5c In the (001) direction there is still a small discrepancy below 1.5 eV, with the calculations overestimating the intensity of the peak around 1 eV, for both ε_1 and ε_2. For ε_1, the calculations overestimate the peak around 1 eV. This feature, already discussed in ref 42 is attributed to the overestimation of the oscillator strengths of the first transition, due to the underestimation of the DFT band gap. This can be corrected by updating the DFT wave functions, for example through self-consistent COHSEX, before the G_0W_0 calculations. In our case, we correct only the energy levels, without updating the DFT wave functions. Despite these deviations, the overall accuracy meets the criteria required for reliable frequency-dependent data in micro- and macro-scale optical response simulations.

As for the reflectivity results, a comparative evaluation of the results from different theoretical approaches reveals that for the (001) polarization state, as shown in Figure 5a,b, the BSE and IPA results are very similar. The IPA spectrum presents a main peak at 1 eV, shifted in the BSE spectrum by an exciton binding energy of 0.1 eV, with essentially the same amplitude, which suggests a Wannier-Mott exciton. This peak is mainly due to transitions between the two bands just below and immediately the above the band gap. In contrast, for the (100) polarization state, the inclusion of local fields and excitonic effects in the BSE calculations leads to a significant improvement in both the ε_1 and ε_2 spectra, compared to the experimental data extracted using the KK transformation. For example, in Figure 5d, the ε_2 spectrum computed with BSE clearly shows a significant improvement in the 1–3 eV range, with respect to the IPA results. In fact, the peak at about 1.4 (1.5) eV seen for the PBE(G_0W_0)/IPA, in the BSE spectra is slightly down shifted in energy by ~0.1 eV and looses intensity, while the peak at 2.5(2.6) eV has its intensity dramatically reduced.

Previously reported theoretical studies on the ε_1 and ε_2 spectra of the M_1 phase for both orientations remain limited in the literature.[40,42,43,45] In the beginning of this section, we compared the reflection spectra from these studies with our calculations and experimental data. Although some theoretical studies show good agreement with Verleur's bulk results in the (001) direction, they fail to achieve the same level of accuracy in the (100) direction. Notably, only one study has reported the ε_2 spectrum using the GW/BSE method, yielding results close to those of Verleur; however, the corresponding ε_1 spectrum was not provided.[40]

We now focus our attention on the R phase. To achieve high accuracy in the calculation of the optical properties of metallic materials, several key factors must be carefully taken into account. These include the description of electronic correlations within DFT-PBE, the accuracy of the random phase approximation (RPA) in capturing interband optical transitions, and the reliability of the model used to describe intraband optical contributions.

As shown in Figure 6, the experimental dielectric function has, for both polarizations, a divergency in the imaginary part (ε_2) below 1 eV whereas the real part (ε_1) presents a very broad peak around 2.5 eV. In the same figure, we show the dielectric function calculated within RPA. The solid blue lines correspond to the interband-only dielectric response, while the dashed green lines include both interband and intraband contributions. The intraband contribution is estimated using the method outlined for bulk metallic MXenes, in ref 59. The

https://doi.org/10.1021/acs.jpcc.5c03003
J. Phys. Chem. C XXXX, XXX, XXX–XXX

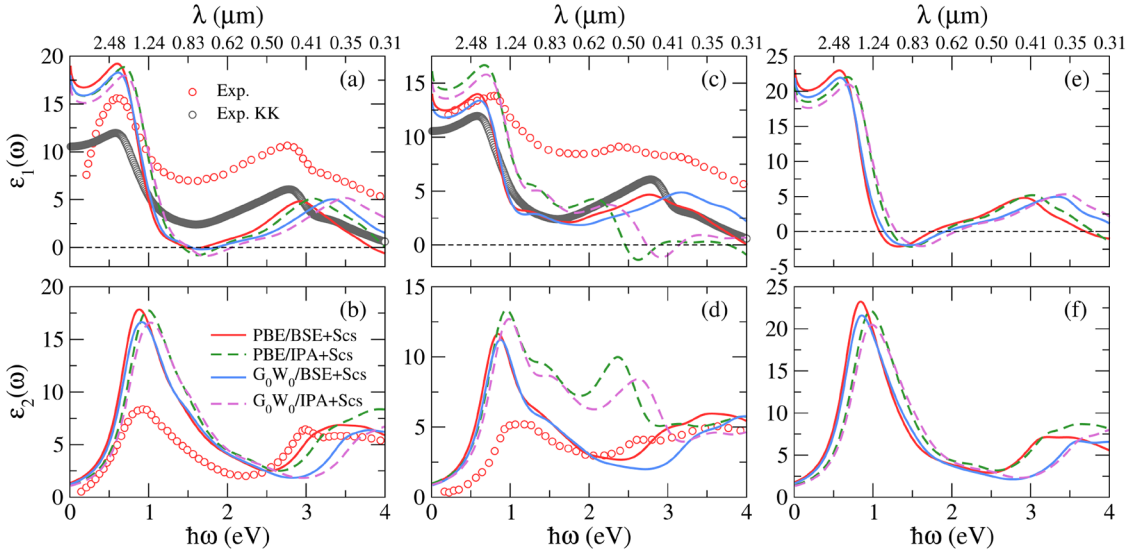

Figure 5. Real and imaginary parts of the dielectric function, calculated for the M_1 phase, for different polarization directions: (001) in panels (a) and (b), (100) in panels (c) and (d), and (010) in panels (e) and (f). The results are obtained using PBE/BSE + Scs (red line), PBE/IPA + Scs (green dashed line), G_0W_0/BSE + Scs (blue line), and G_0W_0/IPA + Scs (pink dashed line) and are compared with experimental data from ref 2. The red circles represent the experimental data for bulk VO_2, while the Kramers−Kronig (KK) result from the experiment is shown as dark gray circles.

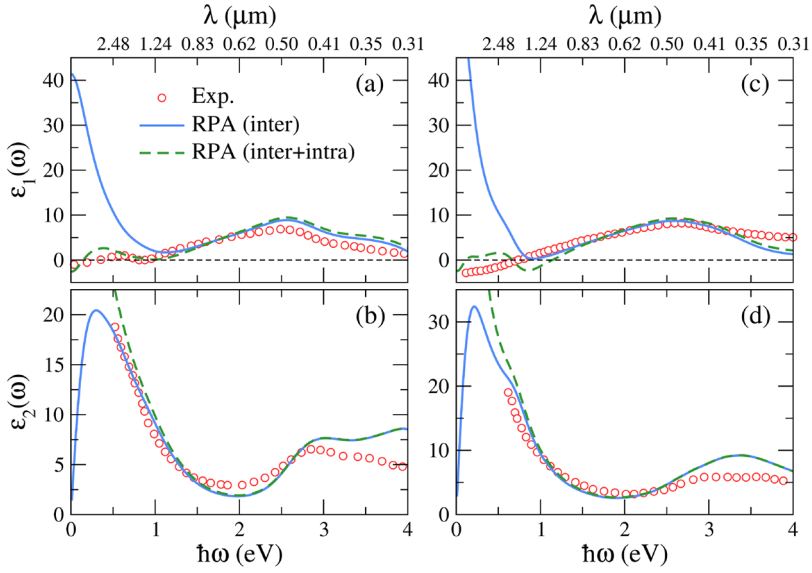

Figure 6. For the R phase, the real and imaginary parts of the dielectric function calculated using RPA are compared with the experimental data (red circles) from ref 2. Panels (a) and (b) show the case where the (100) polarization direction, while panels (c) and (d) correspond to the case where the (001) direction. The solid blue and dashed green lines represent the inter and inter+intra contributions, respectively.

plasma frequency (ω_p) and damping parameter (γ) in the Drude model were predicted to be 1.744 and 0.26 eV, respectively, for the (100) direction, while for the (001) direction, they were found to be 1.714 and 0.21 eV. These values are consistent with the experimentally reported values of ω_p = 1.71 eV and γ = 0.31 eV from Butakov et al.[61]

The results including only the interband contribution (solid blue lines) deviate from the experimental curves in the low-energy region, since they do not reproduce the Drude-like behavior below 1 eV. The inclusion of intraband effects notably improves the agreement with experiment (red circles) in the low-energy region (ω < 1.5 eV), where the Drude-like behavior dominates. In the real part of the dielectric function (ε_1), this is reflected by the more accurate reproduction of the negative slope at low frequencies, whereas in the imaginary part (ε_2), the intra+inter curve captures the broad peak around 1 eV. For the metallic R phase, the dielectric function results clearly meet the accuracy required for utilizing frequency-dependent optical response data in large-scale optical simulations already at the RPA level, as expected for metals.

SUMMARY AND CONCLUSIONS

The optical properties of the M_1 and R phases of VO_2 are critical for understanding temperature-driven phase transitions in technological applications such as smart windows and thermal regulatory coatings. In this study, we investigated the optical properties of both the semiconducting M_1 and metallic R phases. We assessed the accuracy of various theoretical

https://doi.org/10.1021/acs.jpcc.5c03003
J. Phys. Chem. C XXXX, XXX, XXX−XXX

approaches, from DFT to many-body corrections through the GW method and electron−hole interactions through BSE. We were able to reproduce the reported experimental data and clarify several inconsistencies in the existing literature.

For both semiconducting and metal phases, we found the adequate theoretical framework which gives the required accuracy to generate frequency-dependent dielectric data suitable for large-scale optical radiation and light-matter interaction simulations. Our findings indicate that both DFT-PBE and GW band structures, combined with a scissors correction, give similar results for the semiconducting M_1 phase. In order to have a good dielectric function it is however important to go beyond RPA and include excitonic effects through BSE. In contrast, for the metallic R phase, PBE-level/RPA calculations already yield excellent agreement with experimental measurements. It is however important to include the contribution of intraband transitions, in order to reproduce the lower energy part of the spectrum.

To facilitate further research, we provide the computed optical property data for VO_2 in a plain format, available on ZENODO (https://zenodo.org/records/17116270).

■ ASSOCIATED CONTENT

Supporting Information

The Supporting Information is available free of charge at https://pubs.acs.org/doi/10.1021/acs.jpcc.5c03003.

Electronic structure data for VO_2 in both the M_1 and R phases. Specifically, it includes density of states (DOS) and band structure plots calculated using both the PBE and G_0W_0 methods; additionally, a comparative table presents the energy band gap values for the M_1 phase, including both our theoretical calculations and experimental results from the literature (PDF)

■ AUTHOR INFORMATION

Corresponding Authors

Cem Sevik − *Department of Physics and NANOlight Center of Excellence, University of Antwerp, Antwerp B-2020, Belgium*; orcid.org/0000-0002-2412-9672; Email: cem.sevik@uantwerpen.be

Kürşat Şendur − *Faculty of Engineering and Natural Sciences, Sabanci University, Istanbul 34956, Turkey*; Email: sendur@sabanciuniv.edu

Authors

Zafer Kandemir − *Faculty of Engineering and Natural Sciences, Sabanci University, Istanbul 34956, Turkey*

Claudia Cardoso − *S3 Centre, Istituto Nanoscienze, CNR, Modena 41125, Italy*

Pino D'Amico − *S3 Centre, Istituto Nanoscienze, CNR, Modena 41125, Italy*

Complete contact information is available at: https://pubs.acs.org/10.1021/acs.jpcc.5c03003

Notes

The authors declare no competing financial interest.

■ ACKNOWLEDGMENTS

The following computational resources were used in this work: TRUBA, High Performance and Grid Computing Center, funded by the Scientific and Technological Research Council of Turkey (TUBITAK); and UHeM, National Center for High Performance Computing of Turkey under grant number 1019782024. This material is based upon work supported by the Air Force Office of Scientific Research (Aerospace Materials for Extreme Environments Program, PM: Dr. Ali Sayir) under award number FA8655-22-1-7023. This work is supported by the TUBITAK-3501 Career Development Program under grant number 125F085.

■ REFERENCES

(1) Cavalleri, A.; Dekorsy, T.; Chong, H. H. W.; Kieffer, J. C.; Schoenlein, R. W. Evidence for a structurally-driven insulator-to-metal transition in VO_2: A view from the ultrafast timescale. *Phys. Rev. B* **2004**, *70*, No. 161102.

(2) Verleur, H. W.; Barker, A. S.; Berglund, C. N. Optical Properties of VO_2 between 0.25 and 5 eV. *Phys. Rev.* **1968**, *172*, No. 788.

(3) Sawatzky, G. A.; Post, D. X-ray photoelectron and Auger spectroscopy study of some vanadium oxides. *Phys. Rev. B* **1979**, *20*, No. 1546.

(4) Andersson, G.; Parck, C.; Ulfvarson, U.; et al. Studies on Vanadium Oxides. II. The Crystal Structure of Vanadium Dioxide. *Acta Chem. Scand.* **1956**, *10*, 623−628, DOI: 10.3891/acta.chem.scand.10-0623.

(5) Morin, F. J. Oxides Which Show a Metal-to-Insulator Transition at the Neel Temperature. *Phys. Rev. Lett.* **1959**, *3*, No. 34.

(6) Goodenough, J. B. The two components of the crystallographic transition in VO_2. *J. Solid State Chem.* **1971**, *3*, 490−500.

(7) Koethe, T. C.; Hu, Z.; Haverkort, M. W.; Schüßler-Langeheine, C.; Venturini, F.; Brookes, N. B.; Tjernberg, O.; Reichelt, W.; Hsieh, H. H.; Lin, H.-J.; et al. Transfer of Spectral Weight and Symmetry across the Metal-Insulator Transition in VO_2. *Phys. Rev. Lett.* **2006**, *97*, No. 116402.

(8) Qazilbash, M. M.; Brehm, M.; Chae, B.-G.; Ho, P.-C.; Andreev, G. O.; Kim, B.-J.; Yun, S. J.; Balatsky, A. V.; Maple, M. B.; Keilmann, F.; et al. Mott Transition in VO_2 Revealed by Infrared Spectroscopy and Nano-Imaging. *Science* **2007**, *318*, 1750−1753.

(9) Qazilbash, M. M.; Schafgans, A. A.; Burch, K. S.; Yun, S. J.; Chae, B. G.; Kim, B. J.; Kim, H. T.; Basov, D. N. Electrodynamics of the vanadium oxides VO_2 and V_2O_3. *Phys. Rev. B* **2008**, *77*, No. 115121.

(10) Lee, S.; Meyer, T. L.; Sohn, C.; Lee, D.; Nichols, J.; Lee, D.; Seo, S. S. A.; Freeland, J. W.; Noh, T. W.; Lee, H. N. Electronic structure and insulating gap in epitaxial VO_2 polymorphs. *APL Mater.* **2015**, *3*, No. 126109.

(11) Shin, S.; Suga, S.; Taniguchi, M.; Fujisawa, M.; Kanzaki, H.; Fujimori, A.; Daimon, H.; Ueda, Y.; Kosuge, K.; Kachi, S. Vacuum-ultraviolet reflectance and photoemission study of the metal-insulator phase transitions in VO_2, V_6O_{13}, and V_2O_3. *Phys. Rev. B* **1990**, *41*, No. 4993.

(12) Cavalleri, A.; Rini, M.; Chong, H. H. W.; Fourmaux, S.; Glover, T. E.; Heimann, P. A.; Kieffer, J. C.; Schoenlein, R. W. Band-Selective Measurements of Electron Dynamics in VO_2 Using Femtosecond Near-Edge X-Ray Absorption. *Phys. Rev. Lett.* **2005**, *95*, No. 067405.

(13) Choi, S.; Chang, S.-J.; Oh, J.; Jang, J. H.; Lee, S. Electrical and Optical Properties of VO_2 Polymorphic Films Grown Epitaxially on Y-Stabilized ZrO_2. *Adv. Electron. Mater.* **2018**, *4*, No. 1700620.

(14) Barimah, E. K.; Boontan, A.; Steenson, D. P.; Jose, G. Infrared optical properties modulation of VO_2 thin film fabricated by ultrafast pulsed laser deposition for thermochromic smart window applications. *Sci. Rep.* **2022**, *12*, No. 11421.

(15) Chang, T.-C.; Cao, X.; Bao, S.-H.; Ji, S.-D.; Luo, H.-J.; Jin, P. Review on thermochromic vanadium dioxide based smart coatings: from lab to commercial application. *Adv. Manuf.* **2018**, *6*, 1−19.

(16) Ertas Uslu, M.; Yalcin, R. A.; Misirlioglu, I. B.; Sendur, K. Morphology induced spectral reflectance lineshapes in VO_2 thin films. *J. Appl. Phys.* **2019**, *125*, No. 223103.

(17) Fan, L.; Chen, Y.; Liu, Q.; Chen, S.; Zhu, L.; Meng, Q.; Wang, B.; Zhang, Q.; Ren, H.; Zou, C. Infrared Response and Optoelectronic Memory Device Fabrication Based on Epitaxial VO_2 Film. *ACS Appl. Mater. Interfaces* **2016**, *8*, 32971−32977.

(18) Cueff, S.; Li, D.; Zhou, Y.; Wong, F. J.; Kurvits, J. A.; Ramanathan, S.; Zia, R. Dynamic control of light emission faster than the lifetime limit using VO_2 phase-change. *Nat. Commun.* **2015**, *6*, No. 8636.
(19) Lysenko, S.; Rua, A.; Vikhnin, V.; Jimenez, J.; Fernandez, F.; Liu, H. Light-induced ultrafast phase transitions in VO_2 thin film. *Appl. Surf. Sci.* **2006**, *252*, 5512−5515.
(20) Rahimi, E.; Şendur, K. Thermally controlled femtosecond pulse shaping using metasurface based optical filters. *Nanophotonics* **2018**, *7*, 659−668.
(21) Joushaghani, A.; Jeong, J.; Paradis, S.; Alain, D.; Aitchison, J. S.; Poon, J. K. Characteristics of the Current-Controlled Phase Transition of VO_2 Microwires for Hybrid Optoelectronic Devices. *Photonics* **2015**, *2*, 916−932.
(22) Chang, T.; Cao, X.; Li, N.; Long, S.; Gao, X.; Dedon, L. R.; Sun, G.; Luo, H.; Jin, P. Facile and Low-Temperature Fabrication of Thermochromic Cr_2O_3/VO_2 Smart Coatings: Enhanced Solar Modulation Ability, High Luminous Transmittance and UV-Shielding Function. *ACS Appl. Mater. Interfaces* **2017**, *9*, 26029−26037.
(23) Zheng, J.; Bao, S.; Jin, P. TiO_2 (R)/VO_2(M)/TiO_2 (A) multilayer film as smart window: Combination of energy-saving, antifogging and self-cleaning functions. *Nano Energy* **2015**, *11*, 136−145.
(24) Babulanam, S.; Eriksson, T.; Niklasson, G.; Granqvist, C. Thermochromic VO_2 films for energy-efficient windows. *Sol. Energy Mater.* **1987**, *16*, 347−363.
(25) Soltani, M.; Chaker, M.; Haddad, E.; Kruzelesky, R. V. Thermochromic vanadium dioxide smart coatings grown on Kapton substrates by reactive pulsed laser deposition. *J. Vac. Sci. Technol., A* **2006**, *24*, 612−617.
(26) Shi, J.; Zhou, S.; You, B.; Wu, L. Preparation and thermochromic property of tungsten-doped vanadium dioxide particles. *Sol. Energy Mater. Sol. Cells* **2007**, *91*, 1856−1862.
(27) Granqvist, C.; Bayrak Pehlivan, I.; Ji, Y.-X.; Li, S.-Y.; Niklasson, G. Electrochromics and thermochromics for energy efficient fenestration: Functionalities based on nanoparticles of In2O3:Sn and VO_2. *Thin Solid Films* **2014**, *559*, 2−8.
(28) Deb, S. K. Opportunities and challenges in science and technology of WO3 for electrochromic and related applications. *Sol. Energy Mater. Sol. Cells* **2008**, *92*, 245−258.
(29) Granqvist, C. G. Oxide electrochromics: An introduction to devices and materials. *Sol. Energy Mater. Sol. Cells* **2012**, *99*, 1−13.
(30) Yang, Z.; Ko, C.; Ramanathan, S. Oxide Electronics Utilizing Ultrafast Metal-Insulator Transitions. *Annu. Rev. Mater. Res.* **2011**, *41*, 337−367.
(31) Pirouzfam, N.; Abbasi, P. M.; Sendur, K. Inverted optical functionality of phase change material surfaces through Mie resonances of VO_2@Si core−shell structures. *J. Opt. Soc. Am. B* **2024**, *41*, 1936−1946.
(32) Rahimi, E.; Koucheh, A. B.; Sendur, K. Temperature assisted reflection control using VO_2/Si core-shell nanoparticles. *Opt. Mater. Express* **2022**, *12*, 2974−2981.
(33) Dicken, M. J.; Aydin, K.; Pryce, I. M.; Sweatlock, L. A.; Boyd, E. M.; Walavalkar, S.; Ma, J.; Atwater, H. A. Frequency tunable near-infrared metamaterials based on VO_2 phase transition. *Opt. Express* **2009**, *17*, 18330−18339.
(34) Currie, M.; Mastro, M. A.; Wheeler, V. D. Characterizing the tunable refractive index of vanadium dioxide. *Opt. Mater. Express* **2017**, *7*, 1697−1707.
(35) Kana, J. K.; Vignaud, G.; Gibaud, A.; Maaza, M. Thermally driven sign switch of static dielectric constant of VO_2 thin film. *Opt. Mater.* **2016**, *54*, 165−169.
(36) Hiroyuki Abe, H. A.; Terauchi, M. T. M.; Tanaka, M. T. M.; Shin, S. S. S.; Ueda, Y. U. Y. Electron Energy-loss Spectroscopy Study of the Metal-insulator Transition in VO 2. *Jpn. J. Appl. Phys.* **1997**, *36*, No. 165.
(37) Gavini, A.; Kwan, C. C. Y. Optical Properties of Semiconducting VO_2 Films. *Phys. Rev. B* **1972**, *5*, No. 3138.
(38) Guo, Y.; Zhang, Y.; Zhang, L.; Lv, X.; Wu, L.; Cao, Y.; Song, L. Study of the phase transition properties and electronic band structures of VO_2 thin films grown on different substrates. *Mater. Res. Express* **2019**, *6*, No. 026409.
(39) Jayswal, N. K.; Subedi, I.; Shan, A.; Podraza, N. J. Tracking optical properties of VOx films to optimize polycrystalline VO_2 fabrication. *Thin Solid Films* **2024**, *798*, No. 140367.
(40) Varadwaj, A.; Miyake, T. Geometrical-, Electronic- and Optical Properties of Vanadium Dioxide: A Theoretical Perspective from Meta-GGA SCAN. *ChemistrySelect* **2022**, *7*, No. e202200171.
(41) Gatti, M.; Bruneval, F.; Olevano, V.; Reining, L. Understanding Correlations in Vanadium Dioxide from First Principles. *Phys. Rev. Lett.* **2007**, *99*, No. 266402.
(42) Gatti, M.; Sottile, F.; Reining, L. Electron-hole interactions in correlated electron materials: Optical properties of vanadium dioxide from first principles. *Phys. Rev. B* **2015**, *91*, No. 195137.
(43) Eaton, M.; Catellani, A.; Calzolari, A. VO_2 as a natural optical metamaterial. *Opt. Express* **2018**, *26*, 5342−5357.
(44) Xiao, L.; Su, Y.; Qiu, W.; Ran, J.; Liu, Y.; Wu, J.; Lu, F.; Shao, F.; Peng, P. First-principles investigation on solar radiation shielding performance of rutile VO_2 filters for smart windows. *Appl. Phys. Lett.* **2016**, *109*, No. 193906.
(45) Zayed, M.; Elabbar, A.; Yassin, O. Electronic and optical properties of the VO_2 monoclinic phase using SCAN meta-GGA and TB-mBJ methods. *Phys. B* **2020**, *582*, No. 411887.
(46) Giannozzi, P.; Baroni, S.; Bonini, N.; Calandra, M.; Car, R.; Cavazzoni, C.; Ceresoli, D.; Chiarotti, G. L.; Cococcioni, M.; Dabo, I.; et al. QUANTUM ESPRESSO: a modular and open-source software project for quantum simulations of materials. *J. Phys.:-Condens. Matter* **2009**, *21*, No. 395502.
(47) Giannozzi, P.; Andreussi, O.; Brumme, T.; Bunau, O.; Nardelli, M. B.; Calandra, M.; Car, R.; Cavazzoni, C.; Ceresoli, D.; Cococcioni, M.; et al. Advanced capabilities for materials modelling with Quantum ESPRESSO. *J. Phys.:Condens. Matter* **2017**, *29*, No. 465901.
(48) Perdew, J. P.; Burke, K.; Ernzerhof, M. Generalized Gradient Approximation Made Simple. *Phys. Rev. Lett.* **1996**, *77*, No. 3865.
(49) van Setten, M.; Giantomassi, M.; Bousquet, E.; Verstraete, M.; Hamann, D.; Gonze, X.; Rignanese, G.-M. The PseudoDojo: Training and grading a 85 element optimized norm-conserving pseudopotential table. *Comput. Phys. Commun.* **2018**, *226*, 39−54.
(50) Grimme, S. Semiempirical GGA-type density functional constructed with a long-range dispersion correction. *J. Comput. Chem.* **2006**, *27*, 1787−1799.
(51) Wentzcovitch, R. M.; Schulz, W. W.; Allen, P. B. VO_2: Peierls or Mott-Hubbard? A view from band theory. *Phys. Rev. Lett.* **1994**, *72*, No. 3389.
(52) Longo, J. M.; Kierkegaard, P.; Ballhausen, C.; Ragnarsson, U.; Rasmussen, S.; Sunde, E.; Sørensen, N. A. A refinement of the structure of VO_2. *Acta Chem. Scand.* **1970**, *24*, 420−426.
(53) Andersson, G. Studies on vanadium oxides. *Acta Chem. Scand.* **1956**, *10*, 623−628.
(54) McWhan, D. B.; Marezio, M.; Remeika, J. P.; Dernier, P. D. X-ray diffraction study of metallic VO_2. *Phys. Rev. B* **1974**, *10*, No. 490.
(55) Zylbersztejn, A.; Mott, N. F. Metal-insulator transition in vanadium dioxide. *Phys. Rev. B* **1975**, *11*, No. 4383.
(56) Marini, A.; Hogan, C.; Grüning, M.; Varsano, D. yambo: An ab initio tool for excited state calculations. *Comput. Phys. Commun.* **2009**, *180*, 1392−1403.
(57) Sangalli, D.; Ferretti, A.; Miranda, H.; Attaccalite, C.; Marri, I.; Cannuccia, E.; Melo, P.; Marsili, M.; Paleari, F.; Marrazzo, A.; et al. Many-body perturbation theory calculations using the yambo code. *J. Phys.: Condens. Matter* **2019**, *31*, No. 325902.
(58) Salpeter, E. E.; Bethe, H. A. A Relativistic Equation for Bound-State Problems. *Phys. Rev.* **1951**, *84*, No. 1232.
(59) Kandemir, Z.; D'Amico, P.; Sesti, G.; Cardoso, C.; Milošević, M. V.; Sevik, C. Optical properties of metallic MXene multilayers through advanced first-principles calculations. *Phys. Rev. Mater.* **2024**, *8*, No. 075201.

https://doi.org/10.1021/acs.jpcc.5c03003
J. Phys. Chem. C XXXX, XXX, XXX−XXX

(60) Mossanek, R. J. O.; Abbate, M. Optical response of metallic and insulating VO_2 calculated with the LDA approach. *J. Phys.: Condens. Matter* **2007**, *19*, No. 346225.
(61) Butakov, N. A.; Valmianski, I.; Lewi, T.; Urban, C.; Ren, Z.; Mikhailovsky, A. A.; Wilson, S. D.; Schuller, I. K.; Schuller, J. A. Switchable Plasmonic−Dielectric Resonators with Metal−Insulator Transitions. *ACS Photonics* **2018**, *5*, 371−377.

https://doi.org/10.1021/acs.jpcc.5c03003
J. Phys. Chem. C XXXX, XXX, XXX−XXX